



Two new 3d transition metals AlCrCuFeTi and AlCrCuFeV high-entropy alloys: phase components, microstructures, and compressive properties

Jiaojiao Yi¹ · Lu Wang² · Mingqin Xu¹ · Lin Yang²

Received: 17 September 2020 / Accepted: 11 December 2020 / Published online: 6 January 2021
© The Author(s), under exclusive licence to Springer-Verlag GmbH, DE part of Springer Nature 2021

Abstract

Two 3d transition metal high-entropy alloys, AlCrCuFeX (X = Ti, V), were prepared by a vacuum arc-melting, and their phase components, microstructures, and compressive properties were investigated. The phase components of the alloy with X = V were the BCC + FCC dual-phases, while that of the X = Ti alloy was composed of a multi-phase structure (2BCC + FCC + Laves + L2₁). Core-shell structural dendrites, together with discontinuous inter-dendrites formed in the X = Ti alloy, while netlike inter-dendrites surrounded the cellular dendrites in the X = V alloy. Moreover, the X = V alloy possessed a good synergy in strength and plasticity (ultimate strength: 2138 MPa, plastic strain: 7.1%) due to the ameliorating role of the netlike Cu-rich FCC inter-dendrites on the crack extension, while cleavage fracture mechanism for the X = Ti alloy caused by CrTi-rich Laves phase deteriorated its strength and ductility. The high hardness of the AlCrCuFeX alloys with X = Ti and V reaches 714 ± 27 and 565 ± 22 HV, significantly larger than 495 ± 15 HV of the alloy with X = Ni.

Keywords High-entropy alloys · Phase components · Microstructure · Mechanical properties

1 Introduction

Since the concept of high-entropy alloys (HEAs) was proposed by Yeh et al. [1] and Cantor et al. [2] independently in 2004, a vast number of new multicomponent metallic alloys were exploited in succession [3]. These alloys were artificially classified into several HEAs families according to their constituent elements, such as 3d transition metal HEAs (3d TM), refractory HEAs and light metal HEAs, lanthanide (4f) TM HEAs, brasses and bronzes HEAs, precious metal HEAs and interstitial compound HEAs. Of them, 3d TM HEAs gained extensive attention due to their interesting physical and mechanical properties in terms of hardness [4], wear or corrosion resistance [5, 6], high-temperature strength [5] and super plasticity [7]. They usually contain at

least 4 of the 9 following elements: Al, Co, Cr, Cu, Fe, Mn, Ni, Ti, and V. For instance, the 4-element grouping AlCrCuFe occupied around 36% of the reported 3d TM HEAs by Miracle et al. [8]. However, the corresponding compositions of these reported quinary AlCrCuFe-based alloys included only three alloys to date: as-cast AlCrCuFeNi [9], as-sintered AlCrCuFeCo [9, 10] and as-cast AlCrCuFeMnNi [11]. The alloys AlCrFeCu + Ti/V have not been investigated so far.

Many works found that the Ti and/or V incorporation has a great impact on the microstructures and mechanical properties of HEAs. For instance, Wang et al. [12] reported that the phase components changed from a single FCC solid solution of CoCrCuFeNi to a FCC + Laves phase structure of CoCrCuFeNiTi with the yield strength increasing from 230 to 1272 MPa. Moreover, the plastic strain of the CoCrCuFeNiTi_x alloys was inversely proportional to the Ti content. A good synergy in yield strength (2260 MPa) and plastic strain (23%) was acquired for the single-BCC-phase AlCoCrFeNiTi_{0.5} alloy compared to 1373 MPa and 25% for the two BCC dual-phase AlCoCrFeNi alloys [13, 14]. Likewise, Stepanov et al. [15] experimentally showed that the microstructures varied from FCC to FCC + σ for as-cast CoCrFeMnNiV_x HEAs with $x = 0.25 \sim 1$. Meanwhile, a rising trend of the yield strength and hardness, increasing

✉ Lin Yang
yanglin@jsut.edu.cn

¹ School of Mechanical Engineering, Jiangsu University of Technology, Changzhou 213001, People's Republic of China

² School of Materials Science and Engineering, Jiangsu University of Technology, Changzhou 213001, People's Republic of China

from 230 MPa and 144 HV to 1660 MPa and 650 HV, was obtained. Analogously, Chen et al. [16] found that the hardness of $\text{Al}_{0.5}\text{CoCrCuFeNiV}_x$ alloys increased from 204 to 639 HV when the added V reached $x=1$ from the alloy without V addition, with the phase components transforming from FCC to FCC + BCC + σ .

Thus, in this work, considering the advantage of Ti and V on the mechanical properties, Ti and V were added to the 4-element grouping AlCrCuFe to fabricate new HEAs AlCrCuFeX ($X = \text{Ti}, \text{V}$). Afterwards, their phase components, microstructures, and mechanical properties were investigated intensively.

2 Experimental procedures

Ingots of equiatomic AlCrCuFeX ($X = \text{Ti}, \text{V}$) were initially prepared and poured into a $\Phi 4 \times 60$ mm cavity mould (i.e. with the cooling rate of around 800 °C/s) from high-purity raw material (≥ 99.9 wt%) by arc melting in a titanium-getter argon atmosphere. More processing details were reported in our previous work [17]. The actual compositions of the cylindrical samples were measured as $\text{Al}_{19.9}\text{Cr}_{17.8}\text{Cu}_{21.0}\text{Fe}_{20.2}\text{Ti}_{21.2}$ and $\text{Al}_{19.5}\text{Cr}_{20.2}\text{Cu}_{17.8}\text{Fe}_{20.9}\text{V}_{21.5}$ by energy-dispersive spectrometry (EDS), both are close to their nominal compositions. X-ray diffraction (XRD) using PANalytical X'Pert X-ray diffractometer was carried out to profile the phase structures at an identical condition (40 kV, 40 mA, 20–120°, and 3°/min). Their microstructures were analyzed by scanning electron microscope (SEM, Zeiss sigma 500, Germany) equipped with the Electron Backscattered Diffraction (EBSD) detector. Vickers micro-hardness was measured using an HVS-1000B tester under a load of 50 g for 10 s. Their compressive stress–strain curves were acquired by a computer-controlled mechanical testing

machine (Instron, Norwood, MA, USA) at constant ramp speed of 5.6×10^{-3} mm/s and an initial strain rate of 10^{-3} /s. Besides, JMatPro software was used for equilibrium phase diagrams simulations [18]. Phase diagram simulation was carried out by Step Temperature module with a start temperature of 1600 °C, end temperature of 600 °C and step temperature of 10 °C. During the simulation, all possible solid phases were taken into account.

3 Results and discussion

3.1 Phase analysis

The CLAPHAD methodology is powerful to describe the phase formation of conventional binary or ternary alloys [19–22]. For instance, Shafiei et al. [19] discovered that Al–Co–Cr–Fe–Ni alloy belongs to a dual BCC/FCC phase structure by JMatPro. However, for the HEAs exploited recently, the corresponding phase diagrams are commonly unavailable. Thus, in the present work, the equilibrium phase diagram simulated by JMatPro software of the studied two alloys was calculated to predict their phase formation, as shown in Fig. 1. Accordingly, for the studied alloy AlCrCuFeTi, the BCC phase first precipitates from the liquid when the temperature decreases to 1240 °C. Therewith, the α -Cr phase and Laves phase form at temperature below 1080 °C and 1030 °C, respectively. The FCC phase precipitates at the end stage of the solidification process (< 920 °C), in which stage no liquid phase exists. Comparatively, only two phases occur in the entire solidification process of AlCrCuFeV. One is BCC phase forming at 1570 °C, and another is the FCC phase forming below 990 °C. In general terms, no single-phase solid solution is expected in the current studied alloys, implying that the phase components of HEAs

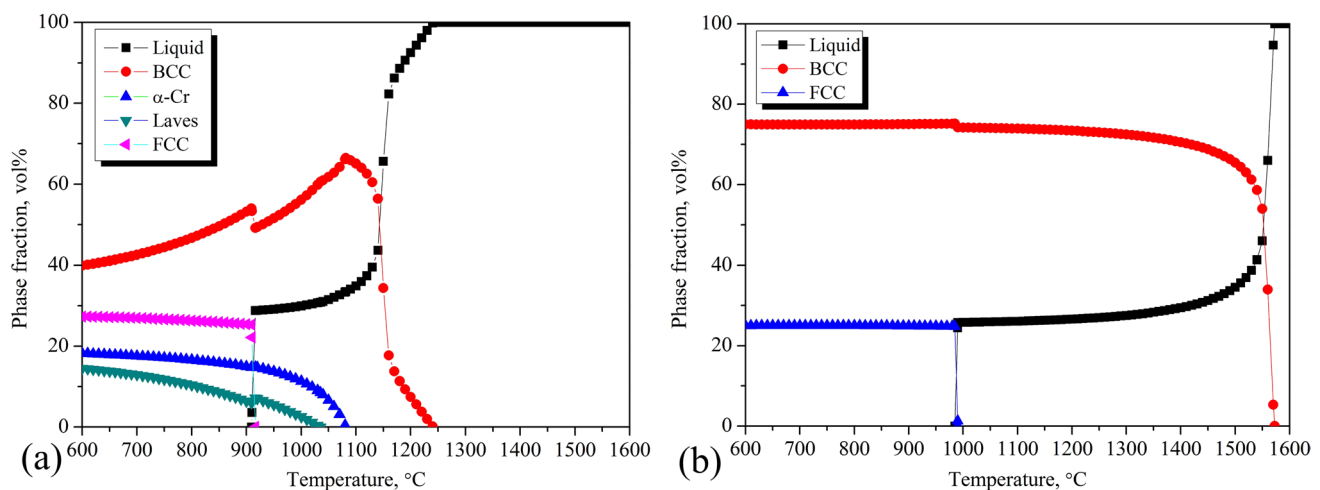


Fig. 1 Simulated equilibrium phase diagrams of the current studied alloys AlCrCuFeTi (a) and AlCrCuFeV (b)

are not only determined by high entropy caused by equal atomic ratio but also by other factors, such as atomic size difference and electronegativity difference [23, 24]. Note that the phase fractions in both the studied alloys tend to be stabilized when the temperature decreases to 600 °C (Fig. 1). Thus, the volume fractions and element concentration of the phases in the studied alloys are predicted as summarized in Table 1 at the temperature of 600 °C. In details, the BCC phase of the AlCrCuFeTi is enriched with Al, Fe and Ti and takes up ~40 vol.%, the α -Cr is enriched with Cr and Al and takes up ~18 vol.%, the Laves is enriched with Fe, Cr and Ti and with a fraction volume of 15%, and the FCC phase is enriched with Cu and Al and with a fraction volume of 27%. For the AlCrCuFeV, the BCC (~75 vol.%) is enriched with Al, Cr, Fe and V, while the FCC (~25 vol.%) is mainly rich in Cu.

The XRD patterns of the AlCrCuFeX (X=Ti, V and Ni [9]) alloys were shown in Fig. 2. Although the XRD pattern of the currently studied AlCrCuFeV was not consistent with that of the reported AlCrCuFeNi, both of them were identified as BCC + FCC dual-phase structures (Fig. 2b, c). Moreover, according to the JCPDS cards, the BCC phase of the AlCrCuFeV corresponded to VCr or VFe BCC phase, while the FCC phase in the alloy (X=V) matched well with the Cu FCC phase, which is common in the Cu-containing HEAs due to the Cu-segregation, such as AlCrCuFeNi, AlCoCrCuFeNi and AlCrCuFeNi₂ [9, 25, 26]. However, the peak's intensity of the FCC phase of the AlCrCuFeV alloy (i.e. X=V) was obviously lower than that of the AlCrCuFeNi alloy (i.e. X=Ni). This is in good agreement with the positive effect of V on the BCC formation concluded by the Chen's investigation [16]. In strike contrast to the AlCrCuFeX alloys (i.e. X=Ni, V), distinct and complicated phase components (i.e., a FeTi BCC (B), a Cu FCC, a Cr BCC' (B'), a Cr-containing hexagonal Laves (γ) and AlCu₂Ti(Cr)-like L2₁ (L) phases) were detected in the alloy AlCrCuFeTi (i.e. X=Ti). The FeTi BCC phase might be the primary phase due to the highest intensities of its peaks, while the Cr-rich BCC' phase is marginal. Note that all the phases but L2₁ were well predicted by the above simulation, which confirmed the simulated reliability and the limitations that depend on the relative databases. The emerged Cr-containing hexagonal Laves phase could be attributed to the

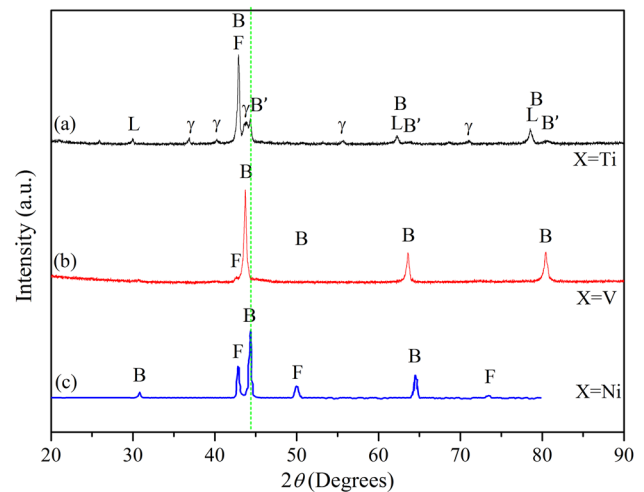


Fig. 2 XRD patterns of the AlCrCuFeX alloys (X=Ti, V, and Ni). Note that the pattern of AlCrCuFeNi was extracted from the Ref. [9]. B and B' represent BCC phases with different lattice constants. F, L and γ represent FCC, L2₁ (Heusler), and hexagonal Laves phases, respectively

high atomic size ratio of the largest (Ti: 1.462 Å) and smallest (Cr: 1.251 Å) elements [14, 27–29], which is actually common for the reported Cr-containing alloys with a large atomic size difference [14]. The AlCu₂Ti(Cr)-like L2₁ phase was similar to AlNi₂Ti-like phase in Al_{0.5}CrFeNiTiV [30], AlCoCrCuNiTiY_x (x=0.5, 0.8, 1) [31], which caused by the high bonding strength among Al, Ti/Cr and Cu. Besides, of these phases, Cu FCC phase was the only common phase in the three alloys (i.e. X=Ti, Ni, V). In addition, the primary peaks of the BCC phases shifted toward to the low-angle side in the order of the alloys with X=Ni, V, and Ti, indicating that the BCC crystal lattice was generally inflated by the order. Convincingly, the lattice constants of the BCC phases were determined as 288.5 pm at X=Ni, to 292.6 pm at X=V and then to 298.8 pm at X=Ti according to the peaks' position and the Bragg's law. The changes in the lattice are likely to be affected by the atomic size of the incorporated elements (Ni: 124.59, V: 131.6, Ti: 146.15 pm). In addition, the lattice constants of each phase in AlCrCuFeX (X=Ti, V, Ni [9]) alloys were calculated and tabulated in Table 2.

Table 1 Calculated volume fractions (in %) and compositions (in at.%) of equilibrium phases in the studied alloys at 800 °C

Compositions	Phases	Al	Cr	Cu	Fe	Ti or V
AlCrCuFeTi	BCC	28.44	3.31	1.29	33.11	33.85
	α -Cr	13.05	85.49	0	1.1	0.36
	Laves	0	21.24	0	45.28	33.48
	FCC	22.92	0.03	71.32	0.03	5.7
AlCrCuFeV	BCC	19.9	26.67	0.1	26.66	26.67
	FCC	20.29	0	79.65	0.04	0

Table 2 Lattice parameters of the component phases of the AlCrCuFeX (X = Ti, V, Ni [9]) alloys

Alloys	Lattice parameters (<i>a/c</i> , pm)					References
	BCC	FCC	BCC'	Hexagonal laves	L2 ₁	
AlCrCuFeTi	298.8	364.5	288.8	423.2/800.9	595.5	This work
AlCrCuFeV	292.6	366.3	–	–	–	This work
AlCrCuFeNi	288.5	365.5	–	–	–	[9]

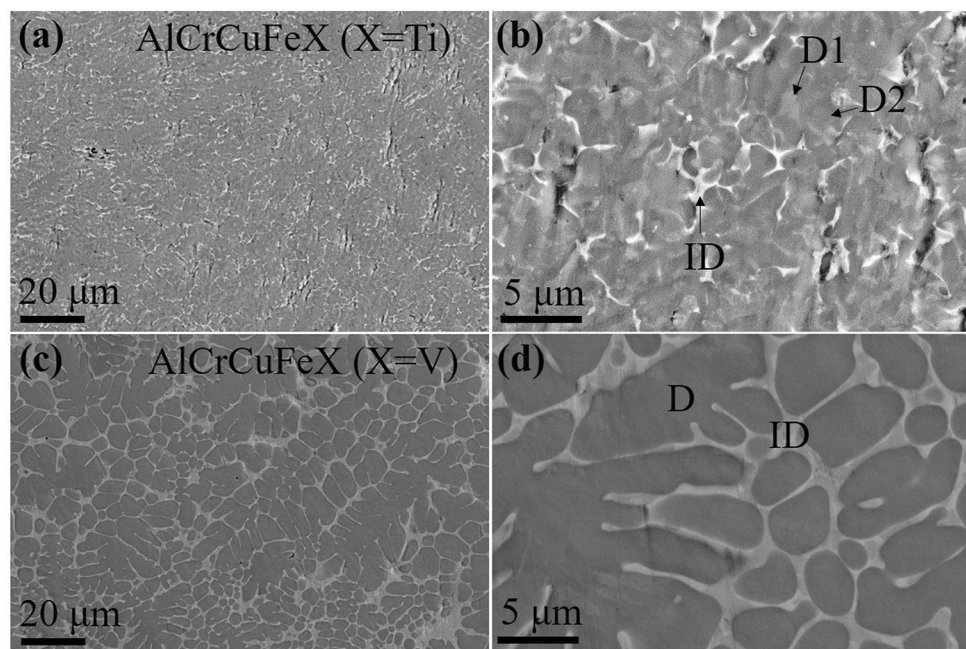
3.2 Microstructures

The microstructures of the currently studied AlCrCuFeX (X = Ti, V) alloys were shown in Fig. 3a–d. When X = Ti, namely the alloy AlCrCuFeTi, three distinct regions were found in the magnified image (Fig. 3b). The bright grey core regions (marked as D1), that distributed in the overall realm randomly, are surrounded by the grey shell regions (marked as D2). In the rest of the regions, discontinuous bright precipitations with several micrometers in length (marked as ID) were separated out. When X = V, namely the AlCrCuFeV alloy, two distinct regions constituted its overall microstructure. Specifically, the cellular dendrites (grey part marked as D in Fig. 3d) taken up the majority of volume fraction and the netlike inter-dendrites (bright part marked as ID) filled the rest of the regions.

Energy-dispersive spectrometry (EDS) mappings of the AlCrCuFeX (X = Ti, V) alloys were carried out to profile their compositional distributions, as shown in Fig. 4. The specific compositions acquired from EDS point scanning were also summarized in Table 3. Note that the elemental distributions of phases are consistent with the simulation results. Accordingly, for the alloy with X = Ti, i.e.

AlCrCuFeTi, its mapping confirmed three distinct regions as observed by the SEM micrograph. More specifically, the D1 regions inside of the dendrite regions were mainly enriched with Cr; while the outside dendrite regions (D2) were enriched with Ti and Fe. Considering the aforementioned phase analysis, we suggested that the D1 regions might be composed of the Cr-rich BCC phase and Cr₂Ti hexagonal Laves phase, and the D2 regions that occupied a large volume fraction, should correspond to the FeTi-rich BCC phase. Interestingly, the inter-dendrites can be actually divided into two different areas according to the EDS point scanning (Table 3) in spite of an indistinguishable SEM micrographs and elemental mapping: one is Cu-rich FCC phase, and another is the AlCu₂Ti(Cr)-like L2₁ phases. For the alloy with X = V, i.e. AlCrCuFeV, the dendrite regions were enriched with Cr, Fe, and V, while the inter-dendrite regions were rich in Cu following by Al, indicating the dendrites and inter-dendrites correspond to VCr + VFe-rich BCC and Cu-rich FCC phases, respectively. Moreover, the Cu-rich FCC inter-dendrite regions seemed to be interconnection forming a netlike framework, consistent with the reported Cu-containing alloys, such as AlCoCrNiCu [32], AlFeNiCuCo [33], and AlCoCrCuFeNi [34, 35], which

Fig. 3 SEM images of the AlCrCuFeX (X = Ti, V) alloys. X = Ti (a, b); X = V (c, d)



were attributed to the Cu segregation resulting from the positive mixing enthalpy among Cu and other principal elements [36]. However, in the currently studied Cu-containing alloy with Ti (AlCrCuFeTi), a discontinuous Cu-rich interdendrites instead of the netlike Cu-rich inter-dendrites in the AlCrCuFeTi alloy formed, which might stem from the AlCu₂Ti formation caused by the active Ti incorporation.

To acquire the volume fraction of each phase, EBSD measurement was carried out, and the representative EBSD maps of the AlCrCuFeV alloy were shown in Fig. 5. Accordingly, the morphology can be divided into yellow, blue and green regions. Hereinto, the yellow regions should be the BCC phase, while the blue regions correspond to the Laves phase. Additionally, the BCC and BCC' phases can hardly

be distinguished by the EBSD method due to their identical crystal structure with different lattice parameters. Thus, the yellow regions should contain the two BCC (BCC and BCC') phases, taking up 67 vol.%. The blue regions associated with the Laves phase take up 25 vol.%. Note that there are around 8 vol.% green regions that commonly represent zero solution of phase analysis. Interestingly, these regions are consistent with the bright precipitations observed in Fig. 5a. Thus, we suggested that the green regions should correspond to the bright Cu-rich FCC phase and AlCu₂Ti-like phases with a total volume fraction around 8%. The zero solution in the green regions might stem from the lattice distortion and residual stress of FCC and AlCu₂Ti-like phases caused by the high degree of solid solution (the Al content in the

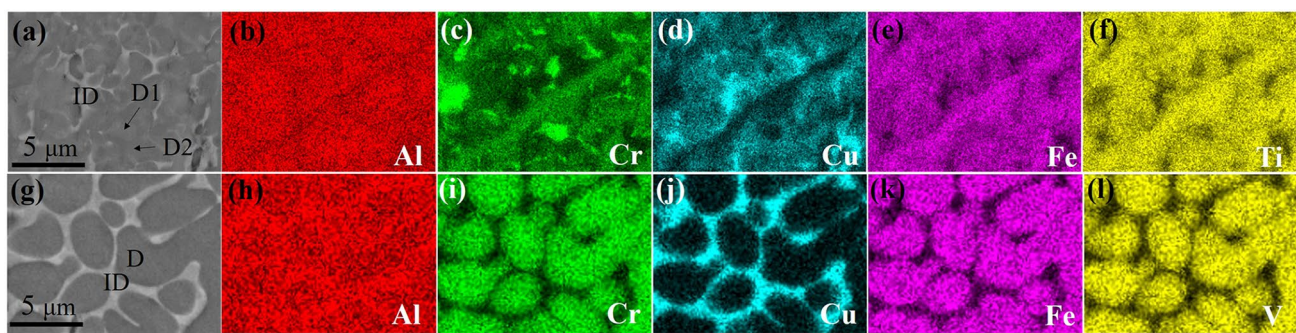


Fig. 4 EDS mappings of the AlCrCuFeX (X=Ti, V) alloys. **a–f** X=Ti; **g–l** X=V

Table 3 Quantitative chemical analysis of the AlCrCuFeX (X=Ti, V) samples (at.%)

AlCrCuFeX	Region	Phase	Al	Cr	Cu	Fe	X
X=Ti	D1	Cr-rich BCC' + Cr ₂ Ti Laves	10.8 ± 1.1	44.4 ± 3.6	8.0 ± 3.5	21.5 ± 1.3	15.3 ± 0.5
	D2	FeTi-rich BCC	13.2 ± 0.8	15.9 ± 2.0	17.4 ± 1.8	25.7 ± 0.5	27.9 ± 0.1
	ID	Cu-rich FCC	13.5 ± 0.2	6.9 ± 2.5	61.2 ± 4.0	8.2 ± 0.7	10.4 ± 0.7
	ID	L2 ₁	13.6 ± 1.0	15.9 ± 5.4	31.6 ± 5.1	18.1 ± 4.2	20.9 ± 5.2
X=V	D	VCr, VFe-rich BCC	15.3 ± 1.2	27.4 ± 1.6	4.1 ± 0.6	24.3 ± 1.1	28.9 ± 1.2
	ID	Cu-rich	26.2 ± 2.9	6.2 ± 2.9	55.3 ± 5.8	6.4 ± 2.7	6.0 ± 3.1

D and ID stand for dendrites and inter-dendrites, respectively

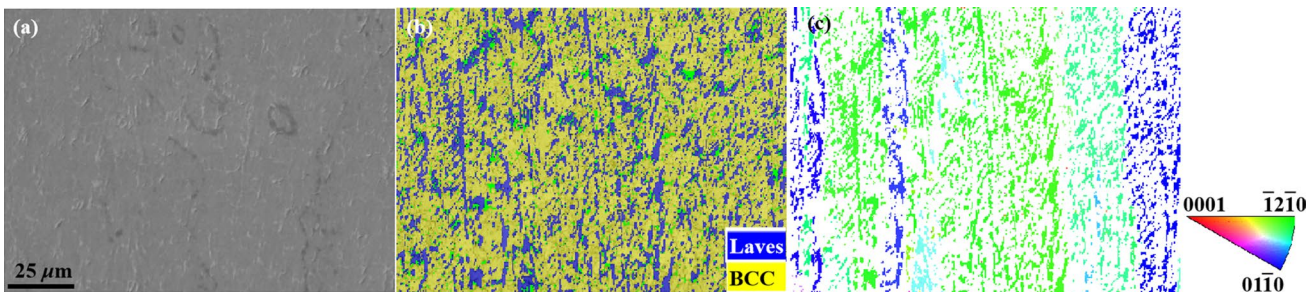


Fig. 5 EBSD maps of the as-cast AlCrCuFeTi alloy: **a** secondary electron (SE) image, **b** phase map of **a**, **c** inverse pole figure (IPF) map of Laves phase in **b** with the standard stereographic triangle on the right

Cu-rich regions is up to 13.5 ± 0.2 at.%). In general, the phase fraction obtained by EBSD is basically consistent with the simulated results: the BCC is the majority phase while the other phase is relatively marginal. Besides, according to the Fig. 5c, it can be found that the Laves phase has strip-like or small particle morphology, and possesses almost the same crystal orientations along the strip direction, such as (01–10) and (–12–10) as confirmed by the standard stereographic triangle. These orientations actually correspond to the low index zone axis, indicating that the studied alloys are likely to be without texture due to the alloys completely solidifying from melting metals.

3.3 Mechanical properties

The compressive engineering stress–strain curves of the AlCrCuFeX (X = Ti, V, and Ni [9]) alloys were shown in Fig. 6a. Compared to the alloys with X = Ti or Ni, the alloy with X = V, i.e. AlCrCuFeV, possessed an outstanding synergy in ultimate compressive strength ($\sigma_b = 2138$ MPa) and plastic strain ($\epsilon_p = 7.1\%$). Besides, the hardness of the alloys with X = Ti and V reaches 714 ± 27 and 565 ± 22 HV, both are significantly larger than 495 ± 15 HV of the alloy with X = Ni and two CrCuFe-based alloys [34, 37], as shown in Fig. 6b. It is well known that the mechanical properties of the alloys strongly depend on their microstructures [38]. For instance, in HEAs, the ductile FCC phases commonly improve an alloy's ductility but undermine its strength [12]. In contrast, greater strength and limited ductility were usually obtained in an alloy with hard BCC/HCP phases [13]. Likewise, the alloys CrCuFeNiCo and CrCuFeNiMo with single FCC phase structure possess the lowest hardness (133 ± 20 , 263 ± 20 HV) (see Fig. 6b), and the other three alloys CrCuFeNiMn, AlCrCuFeNi, and AlCrCuFeV with BCC + FCC dual-phase structure display intermediate

hardness. Moreover, the hardness increases with increasing BCC contents in the three alloys, which confirmed the positive role of BCC content on hardness. However, note that the hardness of AlCrCuFeTi is the largest, even it possesses less amount of BCC phase than AlCrCuFeV. According to the investigation of Ma et al., the hard Laves phase in AlCoCrFeNiNb facilitates the enhancement of the alloy's hardness [14]. Thus, we suggested that the incorporation of ~25 vol.% hard Laves phase might compensate the less BCC phases (tot. 67 vol.%) compared with AlCrCuFeV (~88 vol.% BCC), resulting in high hardness of AlCrCuFeTi.

Typical fracture morphologies of the AlCrCuFeV and AlCrCuFeTi were shown in Fig. 7a–d, respectively. Their features are apparently different. Specifically, for the AlCrCuFeV, a large amount of facets and dimples are noticeable on its fracture surface. Thus, crack is suggested to occur, which rapidly propagated from the relatively brittle BCC phase forming faceted, and then is impeded by the ductile Cu-rich netlike, resulting in the formation of dimples and the larger elongation of 7.1%. In contrast, the fracture feature of AlCrCuFeTi is composed of a typical brittle fracture morphology: cleavage fracture with river patterns and fishbone shape (see Fig. 7c, d). To uncover which phase responsible for the brittle fracture, EDS mapping was carried out on the fracture surface, as shown in Fig. 7e–i. Accordingly, the fishbone or river patterns seems to be always stem from the Cr and Ti-rich regions, which corresponds to CrTi-rich Laves phase according to the phase analysis. Thus, we suggest that the crack might be easily form around the brittle laves phase, and then rapidly propagate along specific force direction, and eventually causes the brittle fracture. In general, the better ductility of the AlCrCuFeV can be attributed to the Cu-rich netlike FCC phase, while the typical brittle fracture of the AlCrCuFeTi is originated from the brittle CrTi-rich Laves phase.

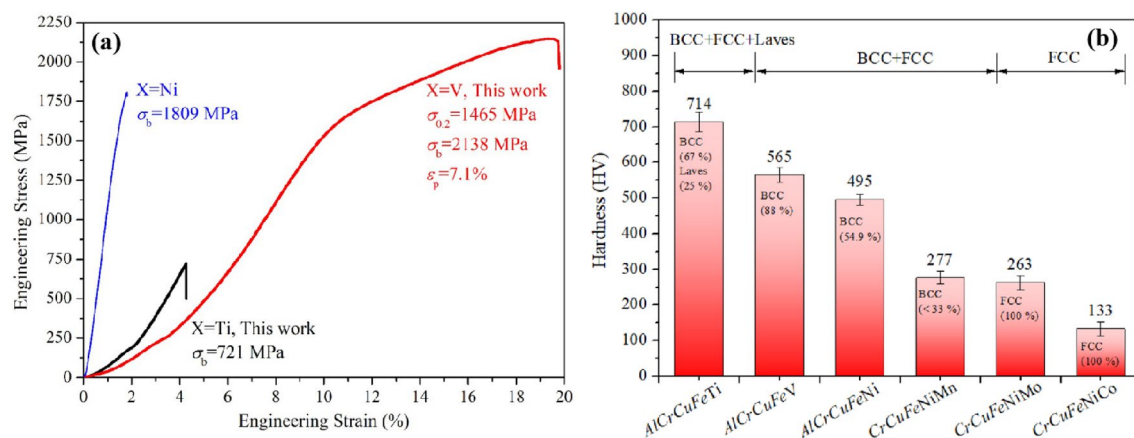


Fig. 6 **a** Engineering stress vs. strain curves of the AlCrCuFeX (X = Ti, V, and Ni [9]) alloys. **b** The hardness and phase constitutions of the AlCrCuFe-base alloys and other quinary equiatomic CrCuFe-base alloys [34, 37]

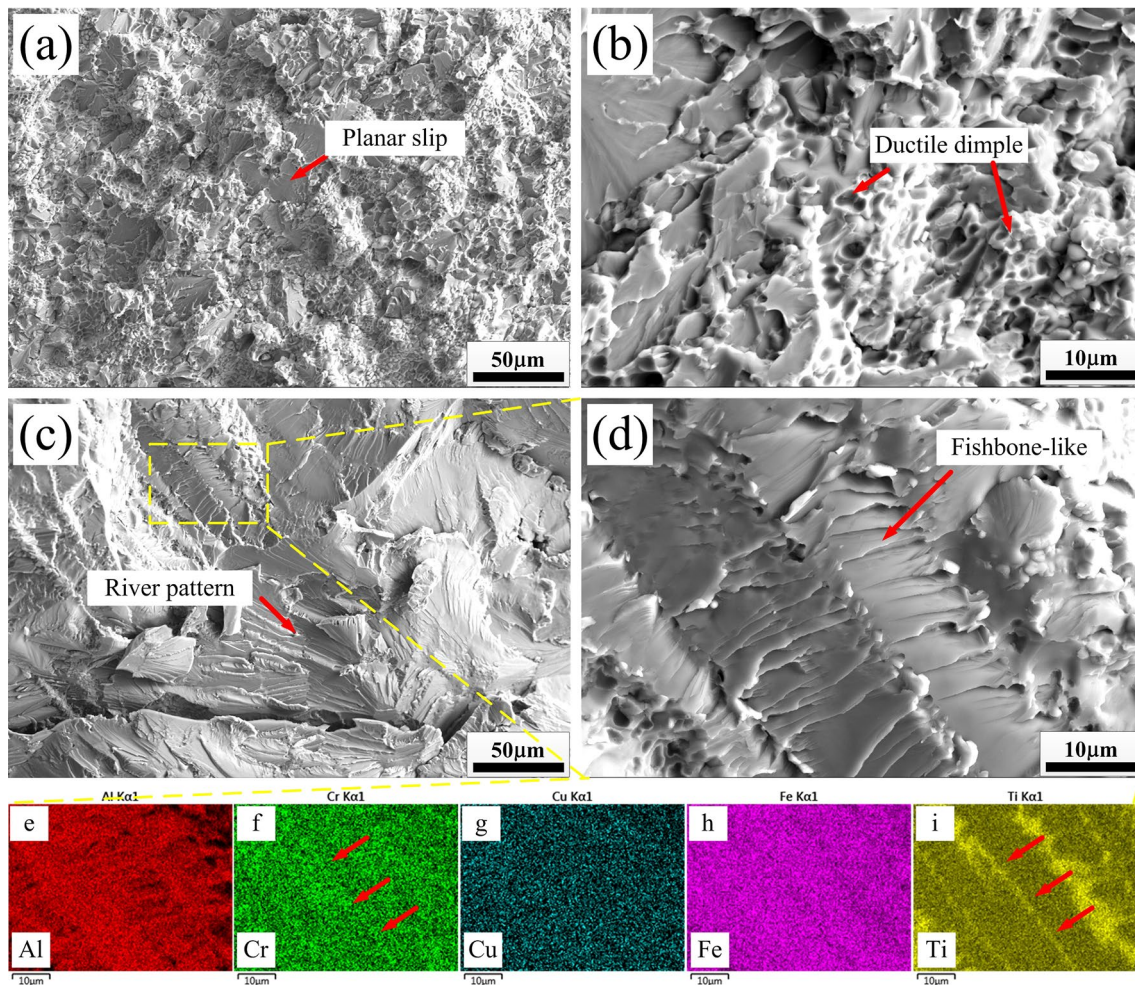


Fig. 7 Fractographic features of AlCrCuFeV (a, b), AlCrCuFeTi (c, d) high-entropy alloys, and corresponding EDS mapping for (c) as displayed in (e–i)

4 Conclusion

In summary, two 3d TM HEAs, AlCrCuFeX (X = Ti, V), were prepared and their phase components, microstructures, and compressive properties are systematically investigated. The following conclusions are reached:

- (1) According to the equilibrium phase diagrams, the phase components of the AlCrCuFeTi are BCC, α -Cr, Laves phase, and FCC phase, while only two phases (BCC + FCC) are formed in AlCrCuFeV.
- (2) The phase components of AlCrCuFeV (i.e. X = V) are composed of the BCC + FCC dual-phases, while that of the alloy with X = Ti, namely AlCrCuFeTi, is more complicated, specifically belonging to two BCC, an FCC, a hexagonal Laves (γ), and AlCu₂Ti(Cr)-like L2₁ phases.
- (3) In AlCrCuFe-based alloy, the V addition is beneficial to the formation of the netlike Cu-rich FCC phase, while the Ti addition deteriorates the Cu segregation and facilitates the emergence of the multi-phase components especially for the brittle CrTi-rich Laves phase.
- (4) An excellent outstanding synergy in ultimate compressive strength ($\sigma_b = 2138$ MPa) and plastic strain ($\epsilon_p = 7.1\%$) was acquired in the alloy with X = V (i.e. AlCrCuFeV), which is attributed to the ameliorating role of netlike Cu-rich FCC inter-dendrites on crack extension.
- (5) The hardness of the AlCrCuFeX alloys with X = Ti and V reaches 714 ± 27 and 565 ± 22 HV caused by the combination of the Laves phase and BCC phase.

Acknowledgements Financial support from the Natural Science Foundation of Jiangsu Province (Grants no. BK20181047) and Natural Science Research of Jiangsu Higher Education Institutions (Grants no. 18KJB430012) are gratefully acknowledge.

Author contributions All authors contributed to the study conception and design. Material preparation, data collection and analysis were performed by JY, LW, MX and LY. The first draft of the manuscript was written by JY and all authors commented on previous versions of the manuscript. All authors read and approved the final manuscript.

Funding Natural Science Foundation of Jiangsu Province (Grants no. BK20181047) and Natural Science Research of Jiangsu Higher Education Institutions (Grants no. 18KJB430012).

Data availability The raw/processed data required to reproduce these findings cannot be shared at this time as the data also forms part of an ongoing study.

Compliance with ethical standards

Conflict of interest The authors declare that they have no known competing financial interests or personal relationships that could have appeared to influence the work reported in this paper.

References

- J.W. Yeh, S.K. Chen, S.J. Lin et al., *Adv. Eng. Mater.* **6**, 299–303 (2004)
- B. Cantor, I.T.H. Chang, P. Knight et al., *Mater. Sci. Eng. A* **375–377**, 213–218 (2004)
- S. Yoshida, T. Ikeuchi, T. Bhattacharjee et al., *Acta Mater.* **171**, 201–215 (2019)
- J.M. Zhu, H.M. Fu, H.F. Zhang et al., *Mater. Sci. Eng. A* **26**, 527 (2010)
- C.Y. Hsu, J.W. Yeh, S.K. Chen et al., *Metall. Mater. Trans. A* **5**, 35 (2004)
- Y.J. Hsu, W.C. Chiang, J.K. Wu, *Mater. Chem. Phys.* **1**, 92 (2005)
- J.Y. He, W.H. Liu, H. Wang et al., *Acta Mater.* **62**, 105–113 (2014)
- D.B. Miracle, O.N. Senkov, *Acta Mater.* **122**, 448–511 (2017)
- J. Pi, P. Ye, Z. Hui et al., *Mater. Sci. Eng. A* **534**, 228–233 (2012)
- S. Praveen, B.S. Murty, R.S. Kottada, *Mater. Sci. Eng. A* **534**, 83–89 (2012)
- V. Soare, D. Mitrica, I. Constantin et al., *Metall. Mater. Trans. A* **46**, 1468–1473 (2014)
- X.F. Wang, Y. Zhang, Y. Qiao et al., *Intermetallics* **3**(15), 357–362 (2007)
- Y.J. Zhou, Y. Zhang, Y.L. Wang et al., *Appl. Phys. Lett.* **18**(90), 181904 (2007)
- S.G. Ma, Y. Zhang, *Mater. Sci. Eng. A* **532**, 480–486 (2012)
- N.D. Stepanov, D.G. Shaysultanov, G.A. Salishchev et al., *J. Alloys Compd.* **628**, 170–185 (2015)
- M.R. Chen, S.J. Lin, J.W. Yeh et al., *Metall. Mater. Trans. A* **37A**, 1363–1369 (2006)
- J. Yi, S. Tang, M. Xu et al., *J. Alloys Compd.* **84**, 156466 (2020)
- Z. Guo, N. Saunders, A.P. Miodownik, *Mater. Sci. Eng. A* **413–414**, 165–169 (2005)
- A. Shafiei, S. Rajabi, *Appl. Phys. A* **125**, 783 (2019)
- G. Liu, L. Liu, X. Liu et al., *Intermetallics* **93**, 269–273 (2018)
- K. Zhang, H. Wen, B. Zhao et al., *Mater. Charact.* **155**, 109792 (2019)
- Z. Cai, G. Jin, X. Cui et al., *Vacuum* **124**, 5–10 (2016)
- S. Guo, C.T. Liu, *Prog. Nat. Sci-Mater.* **21**, 12414 (2011)
- X. Yang, Y. Zhang, *Mater. Chem. Phys.* **132**, 233–238 (2012)
- B.S. Li, Y.P. Wang, M.X. Ren et al., *Mater. Sci. Eng. A* **1–2**, 498 (2008)
- S. Guo, C. Ng, C.T. Liu, *J. Alloys Compd.* **557**, 77–81 (2013)
- F. Otto, Y. Yang, H. Bei et al., *Acta Mater.* **7**, 61 (2013)
- A. Inoue, *Acta Mater.* **48**, 279–306 (2000)
- M. Zhang, X. Zhou, J. Li, *J. Mater. Eng. Perform.* **8**, 26 (2017)
- M.H. Tsai, K.Y. Tsai, C.W. Tsai et al., *Mater. Res. Lett.* **4**, 1 (2013)
- Z. Hu, Y. Zhan, G. Zhang et al., *Mater. Design* **3**, 31 (2010)
- U.S. Hsu, U.D. Hung, J.W. Yeh et al., *Mater. Sci. Eng. A* **460–461**, 403–408 (2007)
- Y.X. Zhuang, W.J. Liu, P.F. Xing et al., *Acta Metall. Sin.* **2**, 25 (2012)
- H.Y. Chen, C.W. Tsai, C.C. Tung et al., *Annales de Chimie Science des Matériaux* **6**, 31 (2006)
- L.H. Wen, H.C. Kou, J.S. Li et al., *Intermetallics* **4**, 17 (2009)
- A. Takeuchi, A. Inoue, *Mater. Trans.* **12**, 46 (2005)
- C. Li, J.C. Li, M. Zhao et al., *J. Alloys Compd.* **1–2**, 475 (2009)
- R. Chen, G. Qin, H. Zheng et al., *Acta Mater.* **144**, 129–137 (2018)

Publisher's Note Springer Nature remains neutral with regard to jurisdictional claims in published maps and institutional affiliations.